Nanoscale

Accepted Manuscript

This article can be cited before page numbers have been issued, to do this please use: Y. Wang, L. Wu, T. I. Wong, M. Bauch, Q. Zhang, J. Zhang, X. Liu, X. ZHOU, P. Bai, J. Dostalek and B. Liedberg, *Nanoscale*, 2016, DOI: 10.1039/C5NR08816J.

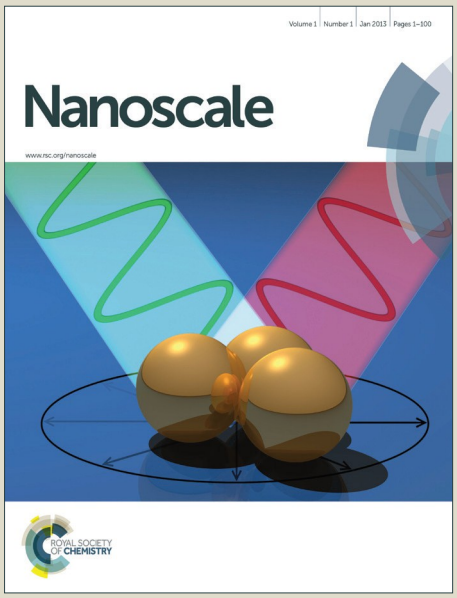

ROYAL SOCIETY OF CHEMISTRY

www.rsc.org/nanoscale

ROYAL SOCIETY OF CHEMISTRY View Article Online
DOI: 10.1039/C5NR08816J

Journal Name

ARTICLE

Directional Fluorescence Emission Co-Enhanced by Localized and Propagating Surface Plasmons for Biosensing†

Received 00th January 20xx,
Accepted 00th January 20xx

DOI: 10.1039/x0xx00000x

www.rsc.org/

Yi Wang,[a,e*] Lin Wu,[b] Ten It Wong,[c] Martin Bauch,[d] Qingwen Zhang,[e] Jinling Zhang,[a] Xiaohu Liu,[a] Xiaodong Zhou,[c] Ping Bai,[b] Jakub Dostalek[d,*] and Bo Liedberg[a,*]

We investigate the simultaneous excitation of localized surface plasmons (LSPs) and propagating surface plasmons (PSPs) on thin metallic film with an array of nanoholes for the enhancement of fluorescence intensity in heterogeneous bioassays. Experiments supported by simulations reveal that the co-excitation of PSP and LSP modes on the nanohole array in a Kretschmann configuration allows for fluorescence enhancement of about 10^2 as compared to a flat Au surface irradiated off-resonance. Moreover, this fluorescence signal was about 3-fold higher on the substrate supporting both PSPs and LSP than that on flat surface where only PSPs were resonantly exited. Simulations also indicated the highly directional fluorescence emission as well as the high fluorescence collection efficiency on the nanohole array substrate. Our contribution attempts de-convoluting the origin of this enhancement and identify further ways to maximize the efficiency of surface plasmon-enhanced fluorescence spectroscopy for implementation in ultra-sensitive bioassays.

Introduction

Surface plasmons (SPs) are optical resonances originating from excitation of free electron oscillations at the surface of metals. They allow for strong electromagnetic field confinement in vicinity to such surfaces which have found diverse applications in analytical technologies,[1, 2] photo-catalysis,[3-6] and opto-electronic devices.[7-10] Besides enabling direct detection of molecular binding events by measuring induced local refractive index changes, plasmonic nanostructures featuring strong enhancement of the electric field intensity offer powerful means for amplifying spectroscopic signal in surface-enhanced Raman scattering (SERS)[11, 12] and metal enhanced fluorescence (MEF).[13-15] The fluorescence emission from emitters such as organic dyes or quantum dots can be enhanced by coupling of their excitation (at wavelength λ_{ab} close to the absorption band) or emission (at emission wavelength λ_{em}) transitions with SPs. The SP-driven excitation at λ_{ab} allows for local enhancement of the excitation rate without increasing the background while the SP-mediated emission can be used to control the angular distribution of emitted light. Highly directional fluorescence emission[16, 17] was demonstrated for the out-coupling of fluorescence light emitted via propagating surface plasmons (PSP) [18, 19] by reverse Kretschmann configuration as well as for the emission mediated by localized surface plasmons (LSPs) supported by plasmonic nanoantennas[20-23]. Up to now, various metallic (nano)structures have been employed for the enhancement of fluorescence emission by combined coupling of emitter absorption and emission with SPs including continuous thin metallic films supporting PSPs,[13] and metallic nanostructures such as nanocubes,[24] nanoholes,[25-28] nanorods,[29, 30] nanodisks,[31] core-shell nanoparticles,[32, 33] DNA-assembled nanoparticles,[34] antennas-in-box[35] and bowtie nanoantennas[36] that support LSPs.[37] The amplified fluorescence signals have been implemented in various bioassays for highly sensitive detection of proteins and nucleic acid analytes[38, 39] with limits of detection (LODs) reaching femtomolar concentration levels. In general, plasmon-enhanced fluorescence biosensors can provide sensitivity that is up to 4 to 5 orders of magnitude better than classical label-free surface plasmon resonance (SPR) biosensors and 1 to 2 orders of magnitude better than ELISA.[40]

Optical excitation of PSPs in the red and near infrared part of spectrum at the surface of noble metals such as gold and silver provides electric field intensity enhancement $|E/E_0|^2$ of ~10-10^2 due to the field confinement in the direction perpendicular to the surface. This confinement can be quantified by the penetration depth L_p (defined as a distance from the metal surface where the surface plasmon electric field amplitude drops by a factor of 1/e) which for PSP equals ~10^2 nm. The field intensity can be further enhanced by engineering PSP modes in order to decrease their Ohmic losses (e.g. long range surface plasmons[40-43]) which translates into an enhancement of fluorescence light intensity by a factor up to EF~10^2. Another efficient means to confine the light intensity and amplify fluorescence signal can be utilized by LSPs that exhibit stronger confinement of the electromagnetic field at distances L_p smaller than a few tens of nanometers. The tighter field confinement of LSPs have been utilized for the amplification of fluorescence intensity which can

[a] Centre for Biomimetic Sensor Science, School of Materials Science and Engineering, Nanyang Technological University, 50 Nanyang Drive, Singapore 637553. E-mail: bliedberg@ntu.edu.sg
[b] Electronics and Photonics Department, Institute of High Performance Computing, Agency for Science, Technology, and Research (A*STAR), 1 Fusionopolis Way, Singapore 138632
[c] Institute of Materials Research and Engineering, Agency for Science, Technology and Research (A*STAR), 3 Research Link, Singapore 117602
[d] .Biosensor Technologies, AIT-Austrian Institute of Technology GmbH, Muthgasse 11, 1190 Vienna, Austria. E-mail: Jakub.dostalek@ait.ac.at
[e] Wenzhou Institute of Biomaterials and Engineering, Chinese Academy of Sciences, Wenzhou, 325001 China. E-mail: wangyi@wibe.ac.cn
†Electronic Supplementary Information (ESI) available: [details of nanostructure design, AFM and calculation of molecular coverage]. See DOI: 10.1039/x0xx00000x

reach an enhancement factor of $EF > 10^2$ for an surface-averaged and even $>10^3$ for individual emitters placed directly at a plasmonic "hot spot".[36] There should be noted that plasmonic hot spot refers to a small volume at which metallic nanostructures confine the electromagnetic field by resonant excitation of LSPs.

In heterogeneous plasmon-enhanced fluorescence bioassays, the surface of metallic (nano)structures is functionalized with biomolecular recognition element (e.g., antibody) that specifically bind target analyte of interest. Typically, the captured analyte is subsequently reacted with another molecule (e.g., detection antibody) that is labelled with a fluorescence emitter (e.g. organic dye, quantum dot). The analyte binding events are detected by monitoring the fluorescence intensity emitted upon probing with confined SP field. Probing by LSPs can lead a substantial enhancement of the fluorescence signal. The enhancement is typically limited by the distribution of the plasmonic hot spots that occupy just a small fraction of sensing spot area. Therefore, the probability of capturing the analyte at the hot spots is low which severely impedes the overall assay sensitivity.

In this paper, the simultaneous excitation of LSP and PSP modes on Au film with an array of nanoholes is investigated for the amplification of fluorescence emission by combining the advantages of LSPs (increased field confinement at hot spots) and PSPs (large surface area that is probed by SP field). Similar structures were studied for other modalities of plasmonic biosensors. For instance, Au nanohole array integrated with nanocone array have shown strong field enhancement through coupling of LSPs.[44] Nanoporous metallic films supporting LSPs and PSPs have been used to study molecular binding events.[45] Similarly, silver nanowell substrates that were prepared from an anodized aluminum oxide template enabled simultaneous excitation of LSP and PSP, in which the PSP was expected to collect the energy of the incident light and re-excite LSP for SERS enhancement.[46] In addition, the coupling of LSP on Au nanoparticles with PSP on Au film was explored for increasing the field intensity in the gaps between a nanoparticle and a metal surface. This approach was reported to provide SERS enhancement up to 10^7,[47] and fluorescence enhancement yielding up to $EF \sim 10^3$.[48] Furthermore, dye molecules placed in a small gap between a silver nanocube and Au film provides highly directional fluorescence emission.[24] However, the use of these approaches for practical applications is limited by the size of the gap. It has to be rather narrow (typically 3~5 nm) which does not allow for accommodating larger molecules such as antibodies and cannot be used for regular assays. We herein investigate fluorescence emission mediated by co-excitation of LSP and PSP modes on Au nanohole arrays in order to tailor it for the amplification in fluorescence bioassays.

Experimental

Materials: The triethylene glycol mono-11-mercaptoundecylether (Thiol-PEG, #673110), PBS buffer tablets, and Tween-20 were purchased from Sigma-Aldrich (Singapore). Biotinylated PEG alkane thiol (Thiol-biotin, #CMT015, HS-$(CH_2)_{10}$-CONH-$(CH_2)_3$-$(OCH_2CH_2)_3$-CH_2-NH-Biotin) was obtained from Nanoscience Instrument, Inc. (USA). Alexa Fluor 647 - labelled streptavidin (SA647, #S21374) was purchased from Invitrogen (Singapore).

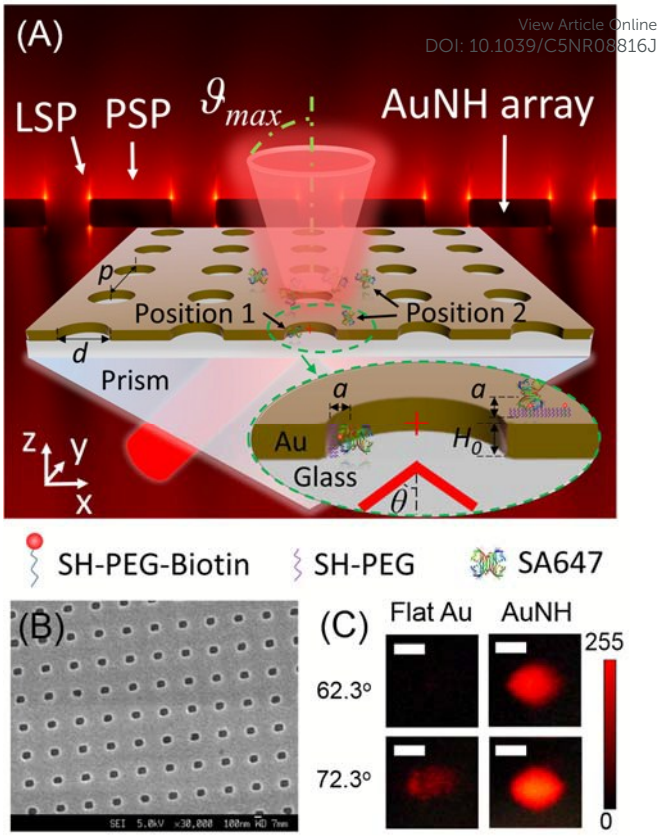

Figure 1. (A) Scheme of the geometry used for co-excitation of PSP and LSP modes on an AuNH array for fluorescence enhancement. The cross symbol "+" indicates the position of x=0, y=0, z=0. ϑ_{max} is the maximal angle of fluorescence emission collected through the optics. (B) SEM observation of nanohole array with a hole diameter of d=150 nm, and pitch of p=400 nm and metallic film thickness of H_0 = 50 nm (5 nm Cr and 45 nm Au). (C) Images of a sensing spot acquired with a CCD camera upon reflection of the excitation laser beam from a flat Au film (left) and AuNH (right) at an angle of incidence of θ=62.3º and 72.3º, respectively. Scale bar 2 mm. The incident angle θ is the angle at the interface between the glass and the Au film.

Optical setup: As shown in Figure 1, an attenuated total reflection (ATR) method was used for the excitation of localized and propagating surface plasmon modes on the sensor surface. A transverse magnetically (TM, p-polarization) polarized beam from a HeNe laser (λ = 632.8 nm) was coupled to a LASFN9 glass prism (n_p = 1.845) for the excitation of LSP and PSP. Onto the prism base, a glass sensor chip (n_g = 1.515) with a structure supporting surface plasmon was optically matched with matching oil (n = 1.700, Cargille lab. NJ, USA). Aqueous samples (with a refractive index close to n_b = 1.333) were pumped at the flow rate of 0.4 mL min^{-1} through the flow-cell using a peristaltic pump. The analyzed samples circulated in the fluidic system with a total volume of 800 µL. The fluorescence light emitted from the sensor surface was collected through the flow-cell by a lens (numerical aperture NA = 0.3), passed through two band-pass filters (transmission wavelength of λ = 670 nm) and its intensity was detected by a photomultiplier tube (PMT) from Hamamatsu (H6240-01, Japan). The LASFN9 glass prism was mounted on a motorized rotation stage and angular reflectivity spectra

$R(\theta)$ were measured by using a photodiode detector and lock-in amplifier.

Sample fabrication: Fabrication of the gold nanohole (AuNH) structures was implemented by nanoimprint lithography with a nickel mold. The nickel mold was fabricated through the electroplating and de-molding of nickel on a silicon mold produced by E-beam lithography. The AuNH array was fabricated with hole pitch p = 400 nm, diameter d = 150 nm, and film thickness H_0 = 50 nm (5 nm chromium and 45 nm of gold). Briefly, the AuNH array were fabricated with an electroplated nickel mold (with nanoholes structure), which was used to nanoimprint the UV curable photoresist layer (mr-UVCur21-300nm from micro resist technology GmbH). The photoresist was then treated with reactive ion etching (RIE) to etch the indented photoresist down to the glass substrate. Afterwards, 5 nm of chromium and 45 nm thick of gold were deposited, and the photoresist was lifted-off by plasma etching and subsequent rinsing with acetone and isopropyl alcohol. For the flat Au film, the glass slides were cleaned in a H_2O:NH_3:H_2O_2 5:1:1 solution at 80 ºC for 5 min, then rinsed with water and dried with N_2 stream. Afterwards, the cleaned glass slides were coated with 2 nm Cr and 47 nm Au by an ultra-high vacuum thermal evaporator (Angstrom, Canada).

Surface modification: For the investigation of Alexa Fluor 647 - labelled streptavidin (SA647) binding, the flat Au film and AuNH substrates were first immersed into a mixed thiol ethanol solution with 0.01 mM Thiol-biotin and 0.09 mM Thiol-PEG overnight. The substrates were dried with N_2 stream before use.

Detection of SA647: The SA647 at concentrations from 0 to 10 nM in PBST buffer (PBS with 0.05% tween-20) were pumped into the flow-cell contact with biotinylated Au substrates for 20 min, followed by 5 min rinsing with PBST for each concentration of SA647.

Simulation of spectra and electromagnetic field distribution: In the simulation, three-dimensional Maxwell's equations were solved using the finite element method (COMSOL Multiphysics). The wavelength-dependent dielectric function of gold was taken from the Palik handbook. The refractive indices for air, water and glass were 1, 1.33, and 1.52, respectively. A unit cell consisting of one nanohole was simulated. At the sides of the unit cell, Floquet periodic boundary condition was assumed in order to obtain the optical response of the whole nanohole array to a light source illuminating from an angle. An obliquely-incident linearly-polarized white light source (400 – 900 nm) was used. As the incident light wave strikes a metal nanohole array, its power will either be absorbed, reflected, or transmitted through the structure. The absorbed power was computed through the volume integration of the resistive heating in the gold nanoparticles, and the reflected or transmitted power was calculated through the surface integration of the far-field power flow. The sum of calculated power of absorption, reflection, and transmission is checked against the incident power to ensure the accuracy of simulation. In addition, the near-field information at the resonant wavelengths in which we are interested can be directly obtained from the simulations.

Simulations of surface plasmon-enhanced fluorescence: Besides the FEM simulations, finite difference time domain (FDTD) method implemented in a commercially available package FDTD Solutions (Lumerical Solutions Inc., Canada) was used. Both FEM and FDTD models allow for the simulation of near field and far field characteristics of investigated plasmonic nanostructures. The comparison of results obtained by these methods allowed for checking their accuracy and validating the data. The fluorescence simulations were carried out assuming a fluorophore placed at a distance of z_0 = 8 nm away from the AuNH and flat Au film surface (Figure 1A). We arrived at that distance by considering the size of streptavidin molecule (~4-6 nm) and the length of the biotinylated PEG alkane thiol (~4.5 nm). A classical fluorescence model was used in which a fluorophore is approximated with oscillating adsorption μ_{ab} and emission μ_e dipoles. In order to calculate the angular distribution of field intensity emitted by a dipole on the surface, a super-cell comprising arrays 49×49 periods was used. The central part including the oscillating dipole was simulated with a mesh size of 1 nm, while the rest of the supercell was simulated with a maximum mesh size of 5 nm. Total emitted power from a dipole P_{em} was calculated by the integration the energy flux through walls of a cube closely surrounding the dipole (cube edge length of 10 nm). Quantum yield of an emitter η that is altered due to the coupling with metallic nanostructures was obtained as a ratio of the energy emitted to the far field P_r and the total emitted energy P_{em}. The energy emitted to far-field was simulated by using a two dimensional detector placed in the plane above and below the nanohole arrays. Near-field components of the electric and magnetic field intensity were recorded and transformed into the far-field dependence of P_r on the polar ϑ and azimuthal φ angles. Considering the surface area of the nanohole wall (i.e. position 1) is much smaller than the gold surface at position 2, the EF was estimated only for the fluorophores located at position 2, Figure 1A.

The excitation rate γ_e of a fluorophore that is irradiated by an incident wave at the absorption wavelength λ_{ab} was assumed as:

$$\gamma_e \propto \left|\vec{E}(\lambda_{ab})\cdot\mu_{ab}\right|^2, \quad (1)$$

which holds for small amplitude of electric intensity $\vec{E}(\lambda_{ab})$ when the excitation rate is far from saturation. Electric field $\vec{E}(\lambda_{ab})$ given in equation (1) was calculated with a single unit cell and a mesh size of 1 nm. After its excitation, the fluorophore returns to its ground state by emitting a photon at a higher wavelength λ_{em} (radiative decay rate γ_r) or without emitting a photon (non-radiative decay rate γ_{nr}). An intrinsic radiative decay rate γ_r^0 and non-radiative decay rate γ_{nr}^0 for an emitter in homogenous aqueous environment exhibit the quantum yield of $\eta_0=\gamma_r^0/(\gamma_r^0+\gamma_{nr}^0)$. When the emitter is brought in vicinity to a metallic structure, decay rates are altered leading to a change in the quantum efficiency η to:

$$\eta=\frac{\gamma_r/\gamma_r^0}{\gamma_r/\gamma_r^0+\gamma_{abs}/\gamma_r^0+(1-\eta^0)/\eta^0}. \quad (2)$$

In Eq. (2), the term γ_r/γ_r^0 states for the normalized radiative decay rate and γ_{abs}/γ_r^0 for additional non-radiative decay rate associated with the absorption by the metal. These ratios can be obtained from FDTD simulations as $\gamma_r/\gamma_r^0=P_r/P_r^0$ and $\gamma_{abs}/\gamma_r^0=(P_{em}-P_r)/P_r^0$, where P_r^0 is the power radiated to far field by identical dipole in homogenous dielectric medium.

The directionality of surface plasmon-coupled emission was taken into account by using a parameter named collection efficiency *CE*. We assume that only light emitted at λ_{em} into a range of polar angles ϑ = 0- ϑ_{max} can contribute to a measurable signal in a realistic biosensor system (e.g., fluorescence light is collected by a lens with a numerical aperture NA=$n\cdot\sin[\vartheta_{max}]$). As following Eq. (3) shows, the *CE* is defined as the emitted power that can be collected within assumed range of polar angles which is normalized to the total power emitted to the far field:

$$CE = \int_0^{2\pi}\int_0^{\vartheta_{max}} P_r(\vartheta,\varphi)\sin\vartheta d\varphi d\vartheta \Big/ \int_0^{2\pi}\int_0^{\pi} P_r(\vartheta,\varphi)\sin\vartheta d\varphi d\vartheta \cdot (3)$$

Results and discussion

The Au structure with arrays of nanoholes was designed for the amplification of fluorescence light emitted by Alexa Fluor 647 which is routinely used in fluorescence assays. This molecule absorbs light at wavelengths centred at λ_{ab}=647 nm and emits maximum intensity of fluorescence light at a peak wavelength of λ_{em}=670 nm. By rational design of the pitch, diameter and thickness of nanohole array arranged in a square lattice, the LSP and PSP resonances were tuned to overlap with λ_{ab} of the emitter. The diameter of nanohole was optimized to 150 nm which provides the highest field enhancement at excitation wavelength λ_{ex} (see Figure S1 in the ESI†).[49-51] The thickness of AuNH was set to 50 nm thereby offering efficient coupling strength to PSPs in the Kretschmann configuration, Figure 1A. The Au structure with the nanohole diameter of 150 nm, pitch of 400 nm, and thickness of the metallic film of 50 nm (5 nm Cr and 45 nm Au) were fabricated on a BK7 glass substrate by using nanoimprint lithography, Figure 1B. The AFM characterization of the AuNH array can be found in Figure S2 in the ESI†.

When brought in contact with an aqueous sample, the AuNH shows two transmission peaks at 645 and 795 nm, respectively, Figure 2A. These resonances were measured for normal incidence (θ=0) and they qualitatively agree with the simulations which indicate that they are accompanied with a confinement of electric field intensity at nanoholes where LSP occurs. Near field simulations predict that the resonance at 645 nm is associated with the enhancement of electric intensity field at the top rim of the nanoholes that is in direct contact with aqueous phase. The resonance at 795 nm shows the enhancement at the bottom rim of the Au nanoholes in contact with the glass substrate. The peak associated with LSPs at the top rim was further used as it allows probing an area that is better accessible to molecules diffusing from the aqueous phase above the structure. The distinct peak at λ=500 nm is due to the interband transition of Au.[52, 53]

By using the Kretchmann configuration, the excitation of LSP and PSP modes was observed by measuring reflectivity at wavelength of λ=632.8 nm upon tuning the incident angle θ. As shown in Figure 2B, the excitation of PSP modes on flat Au and AuNH substrates manifests itself as a dip in reflectivity spectra at similar angles of incidence θ~72º, which qualitatively agrees with simulations. The overall reflectivity change of the AuNH arrays is lower than for flat Au due to the excitation of LSPs at the metallic nanoholes that are not sensitive to variation in the angle of incidence θ. Moreover, the obtained data reveal that the resonance on the AuNH array is significantly broader than for the flat Au film. This is most likely due to radiation losses associated with the diffraction of the periodic array of nanoholes and to a change in the dispersion relation of PSP modes due to the coupling to LSPs. The difference in the coupling angle between the experiment and simulations of the AuNH sample is likely due to the roughness of prepared structures[45] which is not taken into account in the simulations. As shown in Figure 1C, the scattering intensity on the AuNH substrate at the angle of incidence of θ=62.3º (off resonance) and 72.3º (at resonance) were about 10 and 3-fold higher than on flat Au film at the corresponding angles, respectively.

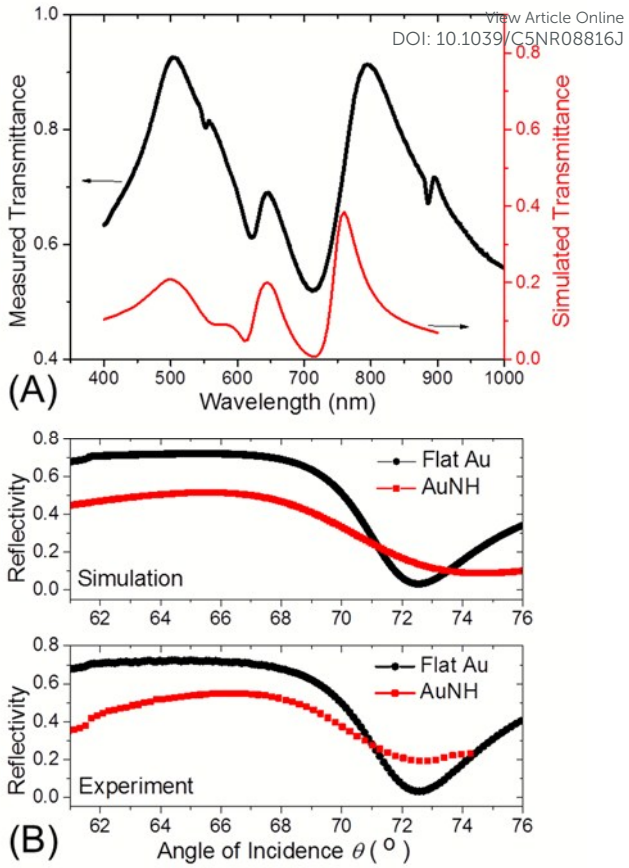

Figure 2. (A) Experimental (black) and simulated (red) UV-vis transmission spectra of the AuNH array on a glass substrate in contact with an aqueous environment. (B) Experimental and simulated angular SPR reflectivity from flat Au and AuNH substrates at a wavelength of λ=632.8 nm.

Finite element method (FEM) simulations were carried out to study the near field enhancement of the electric field due to the excitation of PSP and LSP modes. Figure 3A shows that the excitation of PSP waves at θ=72º on a flat Au film confines the incident field perpendicular to the surface. For the AuNH array under coupling of the incident wave at θ=62.3º, excitation occurs for LSPs located at the upper and lower rim of the Au nanoholes, Figure 3B. When the angle

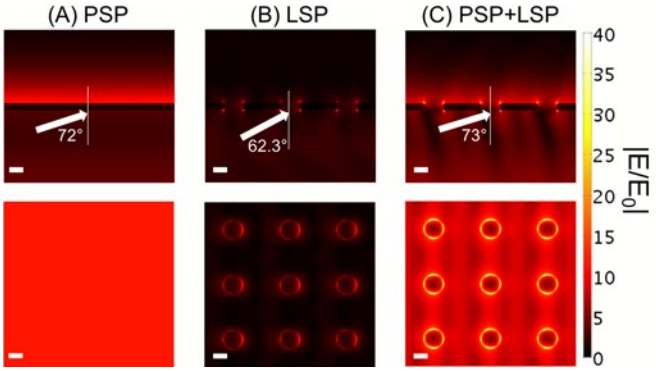

Figure 3. Spatial distribution of electric field amplitude $|E/E_0|$ for (A) resonant excitation of PSP mode on flat Au film, (B) LSP mode on an AuNH substrate and (C) co-excitation of LSP and PSP modes on an AuNH substrate at λ=632.8 nm. The amplitude of the p-polarized plane wave incident at the indicated angles of incidence θ was set to 1. Scale bars are 100 nm.

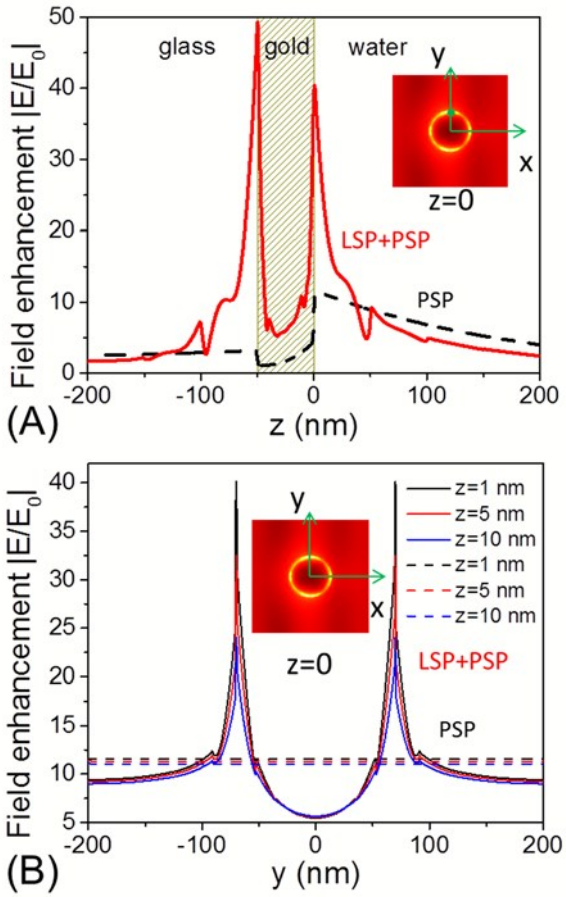

Figure 4. (A) Comparison of cross-sections of the electric field amplitude $|E/E_0|$ as a function of distance z from the surface for the resonant excitation of PSP on flat Au film (dashed) and co-excited LSP and PSP modes on AuNH substrate (solid) at λ=632.8 nm. The field distribution is plotted for x=0 and y=70 nm, green dot (see inset). (B) The cross-section of electric field amplitude $|E/E_0|$ as a function lateral distance along the y-axis (see inset) for different heights above the surface z=1, 5, 10 nm for PSP mode on flat Au film (dashed) and the co-excited LSP and PSP modes (solid) as indicated in the inset figure x=0.

of incidence increases to θ=73º, the PSP and LSP are co-excited which leads to an increase of the field amplitude of LSP, Figure 3C. A maximum field intensity enhancement of $|E/E_0|^2=1.6\times10^3$ is predicted at the rim of the metallic nanoholes upon co-excitation of LSP and PSP modes. This value is about an order of magnitude higher than that of the PSP mode on flat Au film ($|E/E_0|^2$=130) and 8 times higher ($|E/E_0|^2\approx200$) than that observed for excitation of LSPs at the angle θ=62.3º.

In order to explore details of the field enhancement upon coupling to PSP and LSP modes, cross-section of the electric field amplitude $|E/E_0|$ in the vicinity to nanoholes was simulated as presented in Figure 4. These plots show that field amplitude decays exponentially away from the surface for PSP excitation on the flat film, Figure 4A. The co-excitation of PSP and LSP modes at the nanohole rim leads to about 4 times stronger field amplitude at the surface, but the field decays faster away from the surface. For instance, one can see that at distances z larger than ~40 nm from the surface, the field for co-excited LSP and PSP on the AuNH substrate is lower than for the PSP on the flat Au film. Furthermore, Figure 4B displays the lateral field distribution along the y-axis for the excitation of PSPs on a flat Au film and co-excited PSP and LSP at AuNH substrate. It indicates that the field intensity due to co-excited LSP and PSP is stronger than that occurring for the coupling to PSP only in vicinity to the Au nanohole at a perimeter of ~100 nm away from the edge of the nanohole. At distances further away from the hole the flat surface provides stronger field enhancement.

The near field coupling of surface plasmon-enhanced field with emitters that serve as labels in fluorescence assays was studied using FDTD model as described in our previous work.[31] In these simulations the emitters were represented by their absorption and emission dipoles. The angular distribution of fluorescence intensity $P_r(\vartheta,\varphi)$ emitted into the substrate (BK7 glass) and superstrate (aqueous phase) was simulated for the randomly oriented emitters located on the flat Au and AuNH substrate. The distance between emitters and Au surface was set to 8 nm which approximately agrees with the distance between the dye and the surface (see Figure 1). In these simulations, we assumed that only fluorescence light emitted into aqueous medium within a cone defined by the maximum polar angle ϑ_{max}=13º contributes to the signal (corresponding to numerical aperture NA=0.3 of the optics for collecting the emitted light).

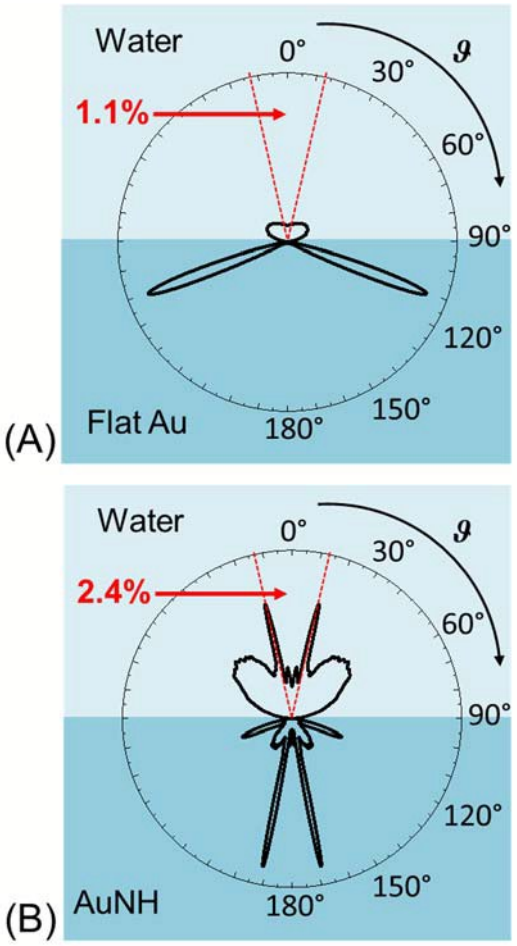

Figure 5. Comparison of the averaged angular distribution of emitted fluorescence intensity $P_r(\vartheta,\varphi=0)$ for emission at the wavelength of λ_{em}=670 nm on (A) flat Au and (B) AuNH substrate. The maximum acceptance polar angles are shown as red dashed lines.

The results presented in Figure 5A show that for a flat Au film the majority of fluorescence light intensity is emitted into the substrate. This is mainly due to the fact that the far field emission strongly couples by near field to PSPs that are subsequently out-coupled via reverse Kretschmann configuration. This leads to the occurrence of a highly directional lobes emitted into the substrate at polar angle ϑ = ±110º. When introducing periodic perforation of the metallic film, diffraction provides competing means for extracting of the emitted light intensity from the surface to the far field. The data in Figure 5B reveals that the lobes associated with reverse Kretschmann out-coupling are suppressed and the emission is dominantly channeled to the far field via diffraction at polar angles of ϑ = ±13º into water and ϑ = ±169º into the glass substrate. The diffraction-coupled emission in water carries the emitted energy predominantly at angles below the acceptance angle ϑ_{max}. From these data, we calculated that a fraction of photons emitted towards aqueous medium at $\vartheta<\vartheta_{max}$ (see Eq. 3) was ~2.2 times higher for the AuNH (collection efficiency, CE = 2.4 %) with respect to the flat Au film (CE = 1.1%).

The model describing the interaction of emitter with the metallic surface was used to predict the overall fluorescence intensity enhancement, that is the product defined as $EF \sim \langle \gamma_e \times \eta \times CE \rangle$ of the enhanced excitation rate γ_e, changed quantum yield η, and collection efficiency CE for random orientation of dyes. The excitation rate γ_e is proportional to the field intensity enhancement $|E/E_0|^2$ at λ_{ex} and the collection efficiency CE quantifies the fraction of photons emitted at λ_{em} that are delivered within the cone defined by the NA (see details in Supporting Information). The intrinsic quantum yield of η^0=0.3 was assumed according to the producer (Life Technologies) for Alexa Fluor 647 dye in water. The simulations reveal that the excitation and emission via co-excited PSP and LSP modes increases the fluorescence intensity F emitted within the NA by a factor of 1.5 with respect to the probing with PSP modes only. Comparing the probing by PSP and LSP (co-excited at θ=72.3º and λ=632.8 nm on AuNH) and by PSP (excited at θ=72.3º and λ=632.8 nm on flat Au film) with that for the probing at off-resonance regime (excited at θ=62.3º and λ=632.8 nm on flat Au film), the fluorescence enhancement by a factor of 72 and 47, respectively, is predicted by the simulations, Table 1.

In order to experimentally evaluate the potential of co-exited LSPs and PSPs for the amplification of fluorescence assay, we prepared substrates with flat Au and AuNH and modified them with a thiol self-assembled monolayer (SAM) containing terminal biotin groups (see Figure 1). These substrates were used for the excitation of either solely PSP or co-exited LSP and PSP modes for probing of

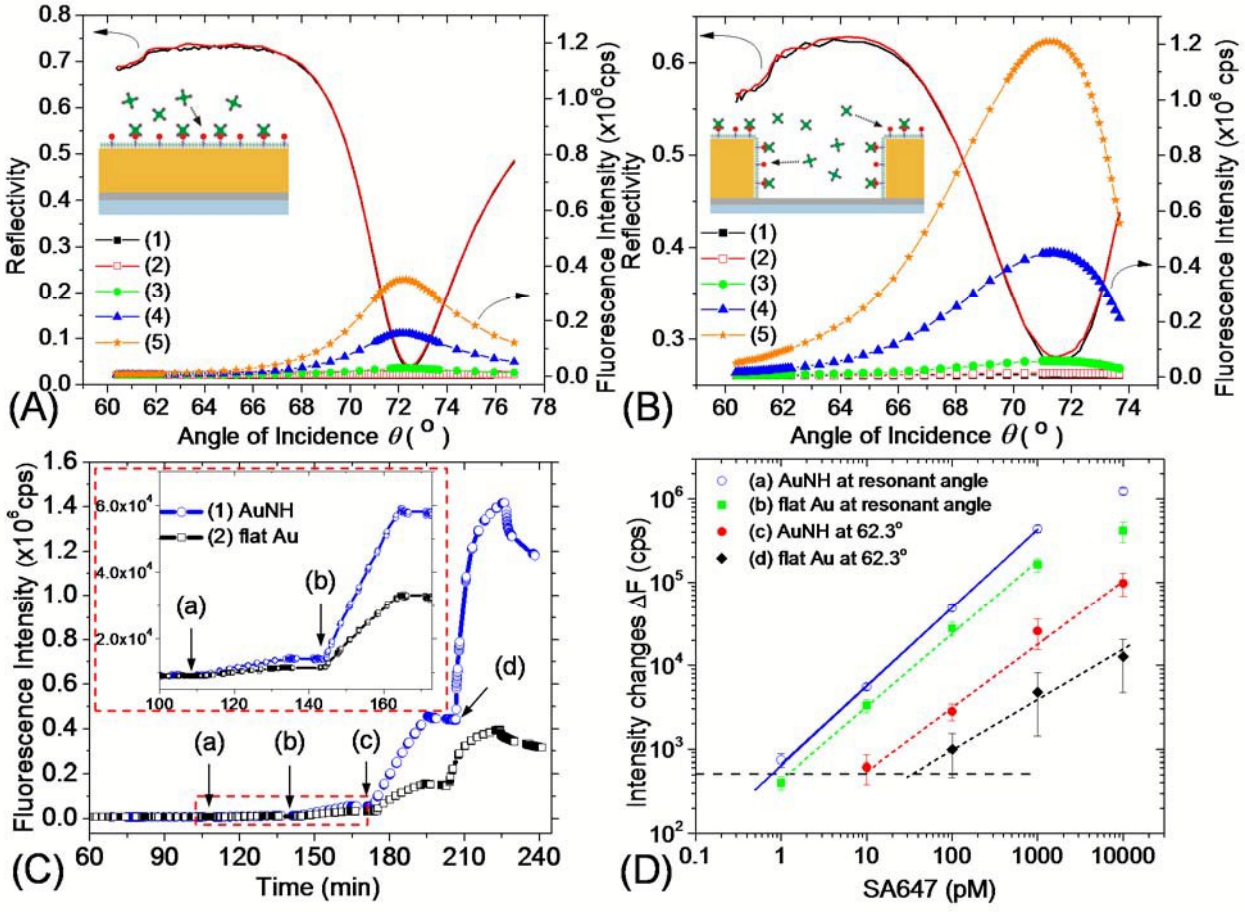

Figure 6. The angular SPR reflectivity (solid lines) and fluorescence spectra (line with symbols) measured on (A) flat Au and (B) AuNH substrates upon the affinity binding of SA647 at concentrations of (1) 0, (2) 10 pM, (3) 100 pM, (4) 1 nM and (5) 10 nM. (C) The kinetics of fluorescence signal on (**1**) AuNH and (**2**) flat Au film upon the sequential binding of SA647 from solutions with a concentration of (a) 10 pM, (b) 100 pM, (c) 1 nM and (d) 10 nM. (D) The fluorescence intensity changes as a function of SA647 concentration on (a) (c) an AuNH array and (b) (d) flat Au film at incident angles of 72.3º and 62.3º, respectively.

Table 1. Fluorescence enhancement *EF* on flat Au and AuNH substrates at different angles of incidence, normalized to the value obtained off resonance at 62.3º for the flat Au.

	Flat Au (72.3º)	AuNH (62.3º)	AuNH (72.3º)
Simulation	47	4.7	72
Experiment	33.3	8.3	100

affinity binding of streptavidin that was labelled by Alexa Fluor 647 dye. The angular SPR reflectivity and fluorescence spectra measured for the flat Au film after binding of SA647 at the concentrations from 10 pM to 10 nM show that the fluorescence intensity *F* increases at the resonant angle θ=72.3º from 4×10^3 to 3.5×10^5 cps , Figure 6A. However, on the AuNH array the affinity binding of SA647 results in a 2-3 times stronger fluorescence signal (from 8×10^3 to 1.2×10^6 cps), Figure 6B.

The fluorescence kinetic measurement at the resonant angle also indicated 2-3 times higher fluorescence intensity changes on AuNH substrates upon the binding of SA647 with respect to the flat Au film, Figure 6C. The fluorescence intensity saturated after incubating SA647 at a concentration higher than 10 nM, which is not the case for the reflectivity measurement. This is due to the high fluorescence intensity which exceeds the linear range and approaches to the maximum detectable intensity (3.6×10^6 cps) of the photomultiplier. The calibration curves for the affinity binding of SA647 on flat Au and AuNH substrates at on-resonant and off-resonant angles are shown in Figure 6D. The limit of detection (LOD) for the detection of SA647 is determined as the concentration of SA647 at which the response is 3 times of the standard deviation of fluorescence fluctuation. The highest sensitivity was achieved on AuNH at on-resonant angle (i.e. upon co-excitation of LSP and PSP) with LOD of 0.7 pM, which is about 2 times and 14 times better than that for the PSP enhanced fluorescence and LSP enhanced fluorescence, respectively. Even though the LSP excited at 62.3º shows the maximum intensity enhancement up to $|E_{sp}/E_0|^2$=200 fold, Figure 3B, which is higher than that of PSP, the LSP enhanced fluorescence shows about 7-fold lower sensitivity, Figure 6D. This is because of the small sensing volume on the AuNH located at the rim of the nanohole.

The experimental and simulated *EF* on flat Au film and AuNH substrate are normalized to the flat Au film at off-resonance angle (62.3º) and summarized in Table 1. The experimental results on AuNH substrate show higher *EF* than expected from the simulations. Note that in the simulation, the molecules located on the wall of the nanoholes were not considered because the wall area is very small in comparison to the overall surface area. In addition, the molecules were assumed to distribute homogenously on the metallic surface.

One may argue that the larger surface area of the AuNH with respect to the flat Au film contributes the fluorescence enhancement. Essentially, the surface area of AuNH substrate can be estimated as $S_{hole} = n(p^2-\pi R^2+2\pi RH_0)$, where *R* and *n* are the radius and the number the nanoholes, respectively. *p* is the pitch of the nanohole array, and H_0 is the thickness of the Au film (see Figure 1). For the same size of flat Au film, the surface area is $S_{flat} = np^2$. Accordingly, the surface area of AuNH is about 1.04 times higher than the Au film. This 4% surface enlargement is too small to explain the 3 times higher fluorescence enhancement on AuNH as compared with flat Au film. The number of streptavidin bound on the AuNH was assumed to be the same as that on the flat Au film, which was estimated to equal 7 to 696 molecules per 400×400 nm^2, after 20 min incubation of 1 pM to 100 pM, respectively, based on fitting the kinetic curves (see Figure S4†). The fluorescence enhanced sensitivity on co-excited LSP and PSP mode is about $G=4.88\times10^{-6}$ cps/molecular, which is about 3.2 times higher than the PSP enhanced fluorescence (see the Supporting Information).

Conclusion

In summary, the co-excitation of LSP and PSP significantly enhances the field intensity which allows for improved fluorescence enhancement when compared to geometries where only individual PSP or LSP modes interact with an emitter. The performed simulations indicate that maximum field enhancement occurs at edges of the nanoholes where emitters are preferentially excited at their absorption wavelength. In addition, highly directional surface plasmon-coupled fluorescence beam at emission wavelength can be observed on AuNH substrate which allows for more efficient extracting of fluorescence light from the sensor surface. The fluorescence measurement upon the binding of Alexa Fluor 647-labelled streptavidin on AuNH substrate revealed a fluorescence enhancement of about 10^2 as compared to a reference flat Au surface irradiated off-resonance. The fluorescence enhancement can be further improved by the selective modification of nanohole array to allow the molecular binding only on the "hotspot" such as the edge of nanohole.[54, 55] We anticipate that this method benefits both the advantages of the stronger electromagnetic field of LSP and longer penetration depth (higher probing volume) of PSP, and the high direction fluorescence emission for ultrasensitive sensing applications. The co-excitation of LSP and PSP has also indicated feasibility for the enhancement of label-free sensors upon detection of biomolecules by monitoring the resonant wavelength shift.[56] In addition, the presented structure for directional surface plasmon-enhanced fluorescence detection can be implemented to a sensor substrate with an open, flow-through, nanohole array design.[57] This design was shown to provide means for more efficient collecting of target analyte on the sensor surface that is not hindered by slow diffusion.[58]

Acknowledgements

The authors thank for the financial support from Science & Engineering Research Council (SERC) of Agency for Science, Technology and Research (A*STAR), for projects under the numbers of 102 152 0014 and 102 152 0015. In addition, this work was partially supported by the Austrian NANO Initiative (FFG and BMVIT) through the NILPlasmonics project within the NILAustria cluster (www.NILAustria.at) and by Austrian Science Fund (FWF) project ACTIPLAS (P244920-N20).

Notes and references

1. J. Homola, *Chem.Rev.*, 2008, **108**, 462-493.
2. J. N. Anker, W. P. Hall, O. Lyandres, N. C. Shah, J. Zhao and R. P. Van Duyne, *Nat. Mater.*, 2008, **7**, 442-453.

3. S. Linic, P. Christopher and D. B. Ingram, *Nat. Mater.*, 2011, **10**, 911-921.
4. S. C. Warren and E. Thimsen, *Energ. Environ. Sci.*, 2012, **5**, 5133-5146.
5. S. Mukherjee, F. Libisch, N. Large, O. Neumann, L. V. Brown, J. Cheng, J. B. Lassiter, E. A. Carter, P. Nordlander and N. J. Halas, *Nano Lett.*, 2013, **13**, 240-247.
6. F. Pincella, K. Isozaki and K. Miki, *Light-Science & Applications*, 2014, **3**.
7. M. W. Knight, H. Sobhani, P. Nordlander and N. J. Halas, *Science*, 2011, **332**, 702-704.
8. W. S. Cai, A. P. Vasudev and M. L. Brongersma, *Science*, 2011, **333**, 1720-1723.
9. Q. Q. Gan, F. J. Bartoli and Z. H. Kafafi, *Adv. Mater.*, 2013, **25**, 2385-2396.
10. N. Liu, F. F. Wen, Y. Zhao, Y. M. Wang, P. Nordlander, N. J. Halas and A. Alu, *Nano Lett.*, 2013, **13**, 142-147.
11. N. P. W. Pieczonka and R. F. Aroca, *Chem. Soc. Rev.*, 2008, **37**, 946-954.
12. J. R. Lombardi and R. L. Birke, *Acc. Chem. Res.*, 2009, **42**, 734-742.
13. T. Neumann, M. L. Johansson, D. Kambhampati and W. Knoll, *Adv. Funct. Mater.*, 2002, **12**, 575-586.
14. J. R. Lakowicz, K. Ray, M. Chowdhury, H. Szmacinski, Y. Fu, J. Zhang and K. Nowaczyk, *Analyst*, 2008, **133**, 1308-1346.
15. M. Bauch, K. Toma, M. Toma, Q. W. Zhang and J. Dostalek, *Plasmonics*, 2014, **9**, 781-799.
16. H. Aouani, O. Mahboub, N. Bonod, E. Devaux, E. Popov, H. Rigneault, T. W. Ebbesen and J. Wenger, *Nano Lett.*, 2011, **11**, 637-644.
17. S. D. Choudhury, R. Badugu and J. R. Lakowicz, *Acc. Chem. Res.*, 2015, **48**, 2171-2180.
18. J. Malicka, I. Gryczynski, Z. Gryczynski and J. R. Lakowicz, *Anal. Chem.*, 2003, **75**, 6629-6633.
19. I. Gryczynski, J. Malicka, Z. Gryczynski and J. R. Lakowicz, *J. Phys. Chem. B*, 2004, **108**, 12568-12574.
20. H. Aouani, O. Mahboub, E. Devaux, H. Rigneault, T. W. Ebbesen and J. Wenger, *Nano Lett.*, 2011, **11**, 2400-2406.
21. T. Ming, L. Zhao, H. J. Chen, K. C. Woo, J. F. Wang and H. Q. Lin, *Nano Lett.*, 2011, **11**, 2296-2303.
22. A. G. Curto, G. Volpe, T. H. Taminiau, M. P. Kreuzer, R. Quidant and N. F. van Hulst, *Science*, 2010, **329**, 930-933.
23. T. H. Taminiau, F. D. Stefani, F. B. Segerink and N. F. Van Hulst, *Nat. Photonics*, 2008, **2**, 234-237.
24. G. M. Akselrod, C. Argyropoulos, T. B. Hoang, C. Ciraci, C. Fang, J. N. Huang, D. R. Smith and M. H. Mikkelsen, *Nat. Photonics*, 2014, **8**, 835-840.
25. A. G. Brolo, S. C. Kwok, M. G. Moffitt, R. Gordon, J. Riordon and K. L. Kavanagh, *J. Am. Chem. Soc.*, 2005, **127**, 14936-14941.
26. X. Q. Cui, K. Tawa, K. Kintaka and J. Nishii, *Adv. Funct. Mater.*, 2010, **20**, 945-950.
27. M. J. Levene, J. Korlach, S. W. Turner, M. Foquet, H. G. Craighead and W. W. Webb, *Science*, 2003, **299**, 682-686.
28. P. F. Guo, S. Wu, Q. J. Ren, J. Lu, Z. H. Chen, S. J. Xiao and Y. Y. Zhu, *J. Phys. Chem. Lett.*, 2010, **1**, 315-318.
29. Y. Fu, J. Zhang and J. R. Lakowicz, *J. Am. Chem. Soc.*, 2010, **132**, 5540-+.
30. S. Khatua, P. M. R. Paulo, H. F. Yuan, A. Gupta, P. Zijlstra and M. Orrit, *ACS Nano*, 2014, **8**, 4440-4449.
31. M. Bauch and J. Dostalek, *Opt. Express*, 2013, **21**, 20470-20483.
32. R. Bardhan, N. K. Grady, J. R. Cole, A. Joshi and N. J. Halas, *ACS Nano*, 2009, **3**, 744-752.
33. K. Sugawa, T. Tamura, H. Tahara, D. Yamaguchi, T. Akiyama, J. Otsuki, Y. Kusaka, N. Fukuda and H. Ushijima, *ACS Nano*, 2013, **7**, 9997-10010.
34. G. P. Acuna, F. M. Moller, P. Holzmeister, S. Beater, B. Lalkens and P. Tinnefeld, *Science*, 2012, **338**, 506-510.
35. D. Punj, M. Mivelle, S. B. Moparthi, T. S. van Zanten, H. Rigneault, N. F. van Hulst, M. F. Garcia-Parajo and J. Wenger, *Nat. Nanotechnol.*, 2013, **8**, 512-516.
36. A. Kinkhabwala, Z. F. Yu, S. H. Fan, Y. Avlasevich, K. Mullen and W. E. Moerner, *Nat. Photonics*, 2009, **3**, 654-657.
37. J. R. Lakowicz, *Plasmonics*, 2006, **1**, 5-33.
38. F. Yu, B. Persson, S. Lofas and W. Knoll, *Anal. Chem.*, 2004, **76**, 6765-6770.
39. D. F. Yao, F. Yu, J. Y. Kim, J. Scholz, P. E. Nielsen, E. K. Sinner and W. Knoll, *Nucleic Acids Res.*, 2004, **32**, e177.
40. Y. Wang, J. Dostalek and W. Knoll, *Biosens. Bioelectron.*, 2009, **24**, 2264-2267.
41. A. Kasry and W. Knoll, *Appl. Phys. Lett.*, 2006, **89**, 101106.
42. J. Dostalek, A. Kasry and W. Knoll, *Plasmonics*, 2007, **2**, 97-106.
43. Y. Wang, A. Brunsen, U. Jonas, J. Dostalek and W. Knoll, *Anal. Chem.*, 2009, **81**, 9625-9632.
44. M. Tabatabaei, M. Najiminaini, K. Davieau, B. Kaminska, M. R. Singh, J. J. L. Carson and F. Lagugné-Labarthet, *ACS Photonics*, 2015, **2**, 752-759.
45. F. Yu, S. Ahl, A. M. Caminade, J. P. Majoral, W. Knoll and J. Erlebacher, *Anal. Chem.*, 2006, **78**, 7346-7350.
46. X. N. Wang, Y. Y. Wang, M. Cong, H. B. Li, Y. J. Gu, J. R. Lombardi, S. P. Xu and W. Q. Xu, *Small*, 2013, **9**, 1895-1899.
47. Y. Liu, S. P. Xu, H. B. Li, X. G. Jian and W. Q. Xu, *Chem. Commun.* , 2011, **47**, 3784-3786.
48. M. Schmelzeisen, Y. Zhao, M. Klapper, K. Mullen and M. Kreiter, *ACS Nano*, 2010, **4**, 3309-3317.
49. Y. Wang, L. Wu, X. Zhou, T. I. Wong, J. Zhang, P. Bai, E. P. Li and B. Liedberg, *Sens. Actuator B-Chem.*, 2013, **186**, 205-211.
50. L. Wu, P. Bai and E. P. Li, *J. Opt. Soc. Am. B*, 2012, **29**, 521-528.
51. J. Zhang, Y. Wang, T. I. Wong, X. Liu, X. Zhou and B. Liedberg, *Nanoscale*, 2015, **7**, 17244-17248.
52. K. L. Shuford, M. A. Ratner, S. K. Gray and G. C. Schatz, *Appl. Phys. B-Lasers O.*, 2006, **84**, 11-18.
53. H. W. Gao, J. Henzie and T. W. Odom, *Nano Lett.*, 2006, **6**, 2104-2108.
54. L. Feuz, M. P. Jonsson and F. Hook, *Nano Lett.*, 2012, **12**, 873-879.
55. L. Feuz, P. Jonsson, M. P. Jonsson and F. Hook, *ACS Nano*, 2010, **4**, 2167-2177.
56. L. S. Live, A. Dhawan, K. F. Gibson, H. P. Poirier-Richard, D. Graham, M. Canva, T. Vo-Dinh and J. F. Masson, *Anal. Bioanal. Chem.*, 2012, **404**, 2859-2868.
57. N. Sharma, H. Keshmiri, X. D. Zhou, T. I. Wong, C. Petri, U. Jonas, B. Liedberg and J. Dostalek, *J. Phys. Chem. C*, 2016, **120**, 561-568.
58. C. Escobedo, A. G. Brolo, R. Gordon and D. Sinton, *Anal. Chem.*, 2010, **82**, 10015-10020.